nature portfolio

https://doi.org/10.1038/s41560-021-00783-z

Supplementary information

Tailoring electrolyte solvation for Li metal batteries cycled at ultra-low temperature

In the format provided by the authors and unedited

Supplementary Information

Tailoring Electrolyte Solvation for Li Metal Batteries Cycled at Ultra-Low Temperature

John Holoubek[a], Haodong Liu[a], Zhaohui Wu[c], Yijie Yin[b] Xing Xing[b], Guorui Cai[a], Sicen Yu[b], Hongyao Zhou[a], Tod A. Pascal[a,b,c,d]*, Zheng Chen[a,b,c,d,]*, Ping Liu[a,b,c,d,]*

[a]*Department of NanoEngineering, University of California, San Diego, La Jolla, CA 92093, USA*

[b]*Program of Materials Science, University of California, San Diego, La Jolla, CA 92093, USA*

[c]*Program of Chemical Engineering, University of California, San Diego, La Jolla, CA 92093, USA*

[d]*Sustainable Power and Energy Center, University of California, San Diego, La Jolla, CA 92093, USA*

Supplementary Discussion 1

Factors dictating solvation structure

The formation of SSIP/CIP structures is ultimately related to the thermodynamic properties of each component, which in the pure solvent case fundamentally defines their physical properties such as melting point, viscosity, dielectric constant, etc. and when salts are introduced play a large role in determining these solvation structures and their subsequent interactions. In this case, the intimate contact between cations and anions in the CIP mode can be thought of a consequence of a lower enthalpic interaction between solvent and cation compared to the SSIP system. It follows that the dissolution of LiFSI in DEE is more entropically dependent than the DOL/DME system, and would thus result in a more facile desolvation process, which is ultimately related to Marcus theory, in which an increase in entropy is favorable for charge-transfer, particularly as the temperature is reduced.[2]

Supplementary Discussion 2

Confirmation of CIP solvation advantage via salt substitution

While the 1 M LiFSI DOL/DME system was observed to display shorting during Li metal plating at low temperature (Figure 2), it is possible that the low temperature Li metal performance of electrolytes employing strongly binding solvents could be improved through altering the solvation structure. For example, when the LiFSI salt was replaced with $LiClO_4$ a resulting CIP electrolyte structure was observed both in MD and Raman analysis (Supplementary Figure 12 a-c). Compared to the 1 M LiFSI DOL/DME system, 1 M $LiClO_4$ DOL/DME also displays a significant reduction in ionic conductivity from 17.0 to 6.36 mS cm^{-1} and a slight increase of transference number from 0.314 to 0.401 (Supplementary Figure 12d,e). Despite this, the critical shorting current was found to increase from < 0.25 mA cm^{-2} in the FSI electrolyte to 2 mA cm^{-2} in the ClO_4 system at -20 ^oC (Supplementary Figure 12g). While these results indicate that the solvation structure can indeed be tailored through the implementation of new anions using ostensibly poor solvents, the development of such anions that are simultaneously stable with Li metal still presents a significant challenge. In this case the 1 M $LiClO_4$ DOL/DME electrolyte was found to produce a Li metal CE of 89.5 % at 23 ^oC, which renders it untenable for practical LMBs (Supplementary Figure 12h).

Supplementary Discussion 3

Confirmation of monodentate ether advantages

To further substantiate the claims made by this work, the improved Li metal performance at low temperatures has also been observed in dipropyl ether (DPE) and dibutyl ether (DBE). These monodentate ethers have also been simulated to produce a CIP electrolyte structure similar to the DEE system (Supplementary Figure 13a,b). Additionally, these electrolytes were found to produce comparable Li metal reversibility at ultra-low temperatures, displaying a CE values of of 97.3% 98.2%, respectively at -40 ^{o}C (Supplementary Figure 13c). These systems indicate that DEE is not a singular case, and that other systems with a CIP solvation structure, relatively weak Li^{+}/solvent interactions and high intrinsic Li metal stability at room temperature produce similar performance metrics at low temperature.

Supplementary Discussion 4

Examination of LMB shorting induced via temperature and bulk transport in SSIP and CIP systems

It is crucial to note that the solvation trends described in this work do not imply that bulk ionic transport is unimportant to low-T operation, rather that both sufficient transport, *and* interphasial kinetics must be addressed for reversible Li plating at ultra-low temperature. To illustrate this, we have demonstrated the difference between Li shorting due to mass transport and desolvation through a study of various concentrations of LiFSI in DEE and DOL/DME (Supplementary Figure 14,15). These systems were found to maintain comparable transference numbers at 0.1 M and 0.5 M LiFSI, while the 0.1 M systems were found to present significantly reduced ionic conductivities and therefore Sand's capacities than their 0.5 M and 1 M counterparts (Supplementary Figure 14,15). As the chemical components of these systems are identical, and the transference numbers indicate no shift in solvation structure, analyses of the performance of these systems allows for the alteration of the bulk ionic transport properties while maintaining the desolvation mechanics.

A summary of the critical current of each concentration is shown in (Supplementary Figure 16), where the critical current of FSI-DOL/DME systems was found to 2 mA cm^{-2} for the 0.1 M electrolyte, while the 0.5 M and 1 M systems exceeded 5 mA cm^{-2}. While this indicates there is indeed a mass transport limitation at low concentrations, all three of the investigated FSI-DOL/DME concentration series were found to short at 0.25 mA cm^{-2} when the temperature was

reduced to -20 ^{o}C and below. This strong correlation between the temperature and the critical current despite similar Sand's Capacities across temperature (Supplementary Figure 7, 14c-e) once again supports that the desolvation kinetics define the shorting behavior of the FSI-DOL/DME electrolyte systems. Conversely, the FSI-DEE concentration series (Supplementary Figure 15) was found to present a weak correlation between temperature and the critical current, where the performance at low temperatures were far superior to the DOL/DME systems. Instead, the DEE series critical currents were found to be almost entirely defined by the salt concentration, implying that the lower ionic conductivity of these systems become problematic for practical performance at low salt concentration. While these results clearly indicate that sufficient bulk ionic transport is indeed necessary for ultra-low temperature LMB electrolytes, the interphasial kinetics are a vital factor to overcome to enable reversible performance. In this regard, the tailoring of the electrolyte solvation structure is crucial.

Supplementary Discussion 5

Li||SPAN pouch cell demonstration and shorting experiment

It is worth noting that depending on the application for a given system the safety should also be considered. To provide a first-step in demonstrating the scalability and potential safety risks associated with LMBs at ultra-low temperature, we have assembled a 160 mAh Li||SPAN pouch cell utilizing a further increased cathode loading of 6 mAh cm^{-2} (Supplementary Figure 23a). This pouch cell was able to produce a capacity of 450 mAh g^{-1} when charged and discharged at -40 ^{o}C, which compares favorably to the coin-cell performance given the increased loading and overall cell size (Supplementary Figure 23b). Furthermore, when put under soft-shorting conditions at -40 ^{o}C, the cell temperature was found to change negligibly, indicating that this process may not result in catastrophic outcomes at such operating temperatures (Supplementary Figure 23c).

Supplementary Table 1. Physical properties of the investigated solvents obtained from ref. 1.

Solvent	Melting Pt.	Boiling Pt.	Viscosity (25 ºC)	Dipole Moment	Dielectric Const.
1,2- Dimethoxyethane **(DME)**	-58 ºC	85 ºC	1.1 cP	1.71 D	7.2
1,3 Dioxolane **(DOL)**	-95 ºC	75 ºC	0.589 cP	1.19 D	7.34
Diethyl Ether **(DEE)**	-117 ºC	35 ºC	0.224 cP	1.3 D	4.33

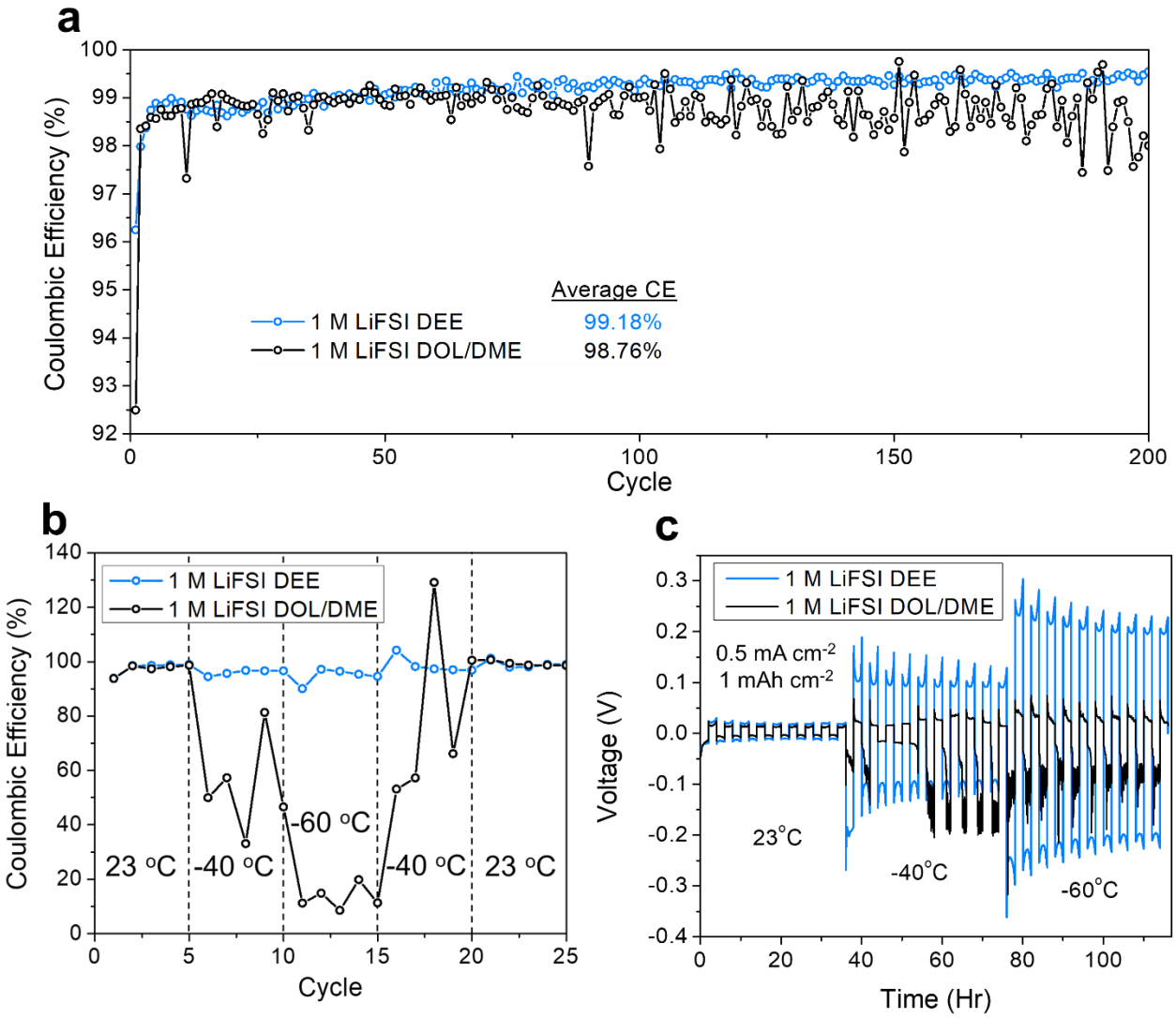

Supplementary Figure 1. Extended Li metal performance in the electrolytes of interest. **a)** extended plating/stripping efficiency of the electrolytes at 0.5 mA cm^{-2} and 1 mAh cm^{-2}. **b)** continuous plating/stripping efficiency of the investigated electrolytes under varying temperature conditions. **c)** Plating/stripping curves of the investigated electrolytes in symmetric Li||Li cells at various temperatures. The unstable voltages displayed by the DOL/DME system are attributed to soft shorting events.

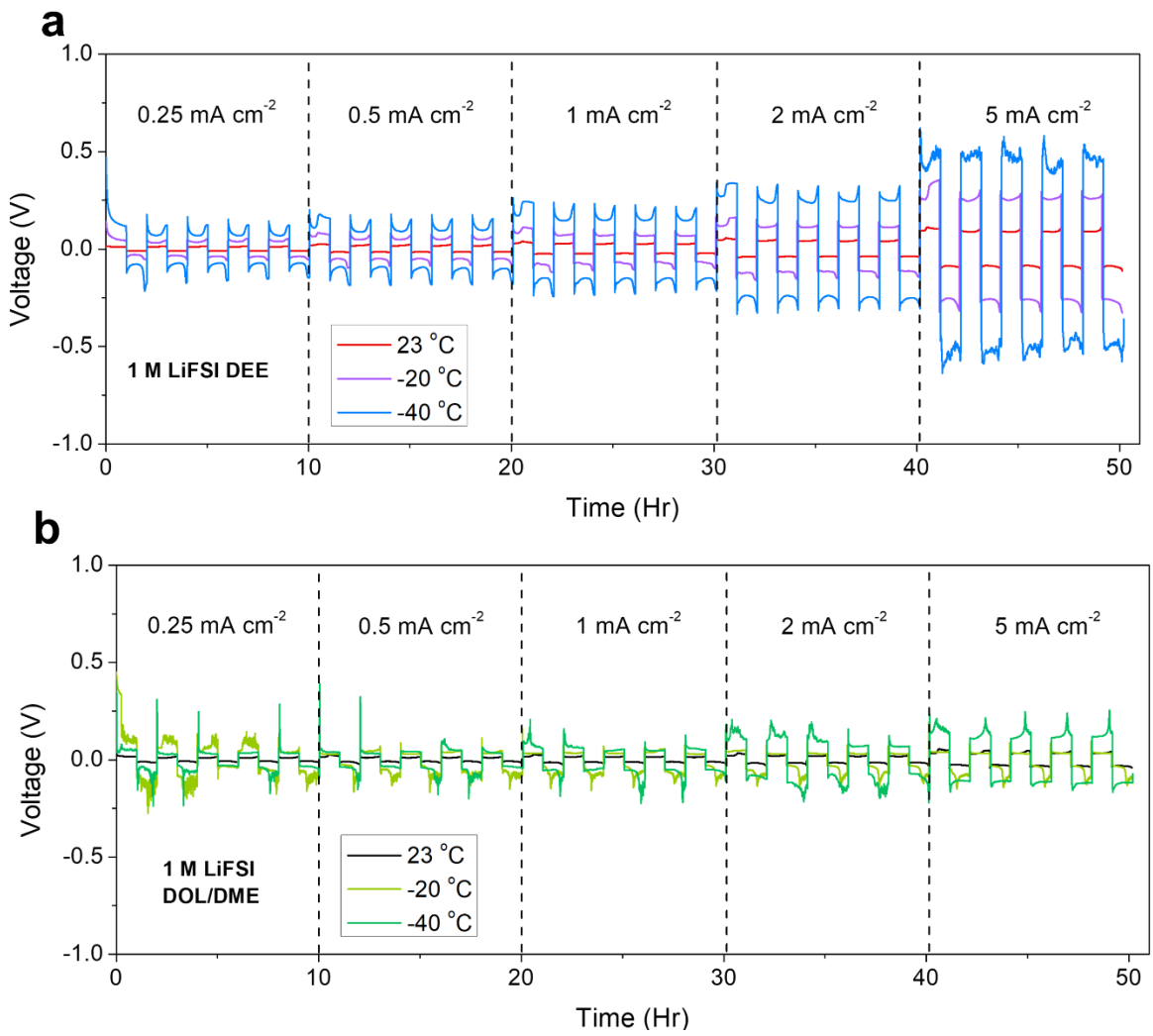

Supplementary Figure 2. Plating/stripping curves in symmetric Li||Li cells at various temperatures and rates in **a)** 1 M LiFSI DEE and **b)** 1 M LiFSI DOL/DME. The unstable voltages displayed are attributed to soft shorting events.

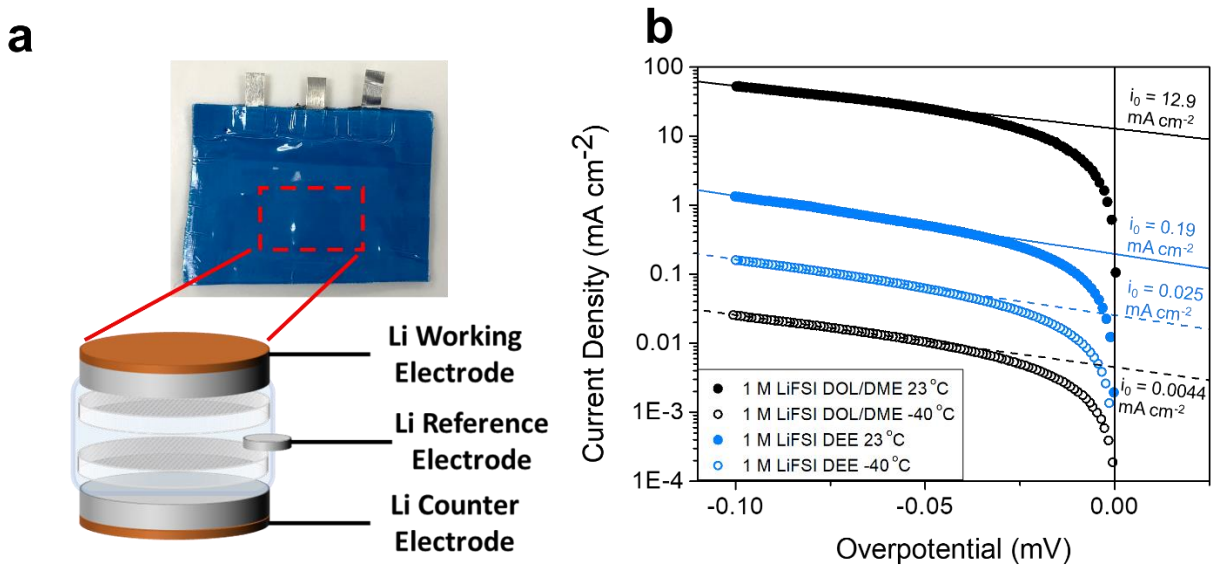

Supplementary Figure 3. 3-Electrode Tafel measurements for Li plating in selected electrolytes. **a**) Photo and schematic of 3 electrode Li||Li||Li cells **b)** Tafel plots of the selected electrolytes at room temperature and -40 ^{o}C using LSV at 1 mV s^{-1}.

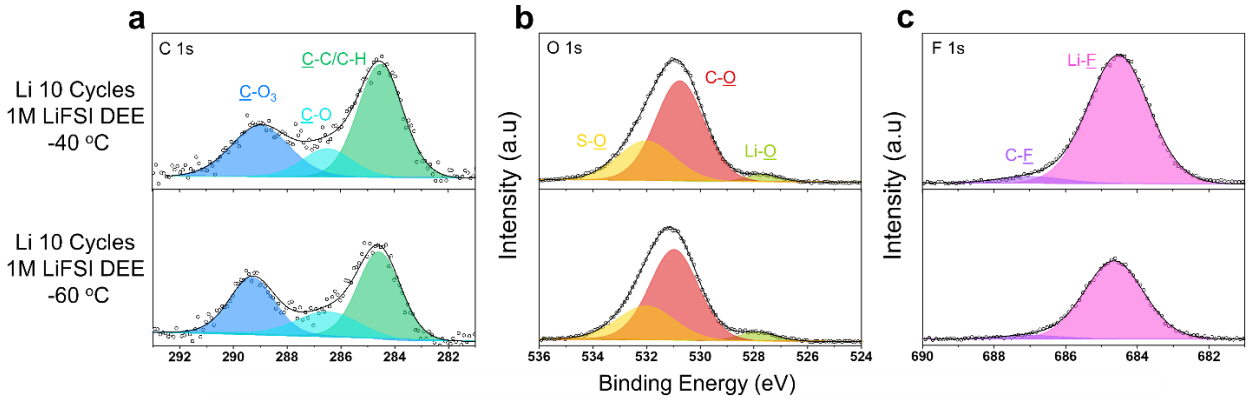

Supplementary Figure 4. Ex-situ XPS of Li anodes after 10 cycles for 1 mAh cm^{-2} at 0.5 mA cm^{-2} in 1 M LiFSI DEE at -40 °C and -60 °C. **a)** C 1s, **b)** O 1s, and **c)** F 1s spectra. The DOL/DME system was not considered at -40 °C and -60 °C due to the shorting issue.

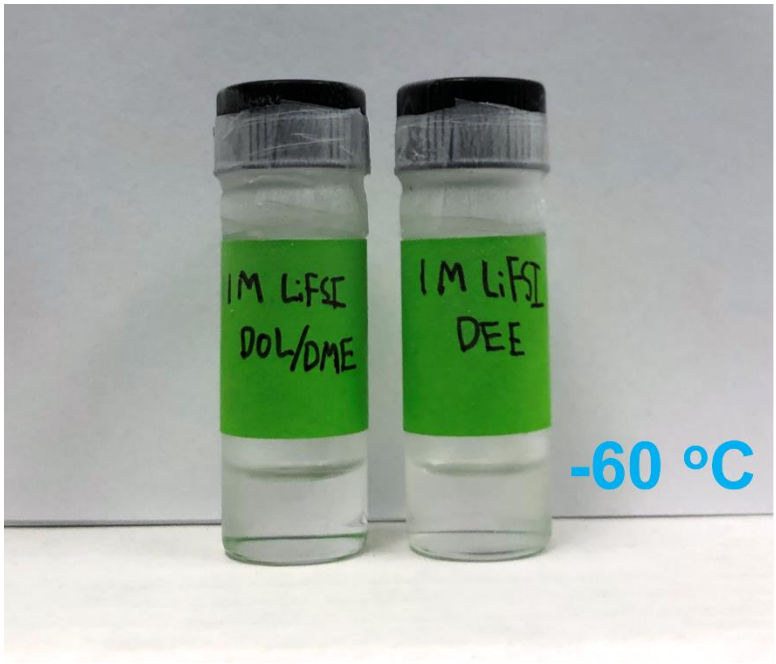

Supplementary Figure 5. Photo of the investigated electrolytes at -60 ºC.

Supplementary Table 2. Comparison of theoretical and experimental transference numbers.

Electrolyte	Experimental t_+	t_+ from MD
1 M LiFSI DOL/DME	0.314	0.333
1 M LiFSI DEE	0.512	0.511

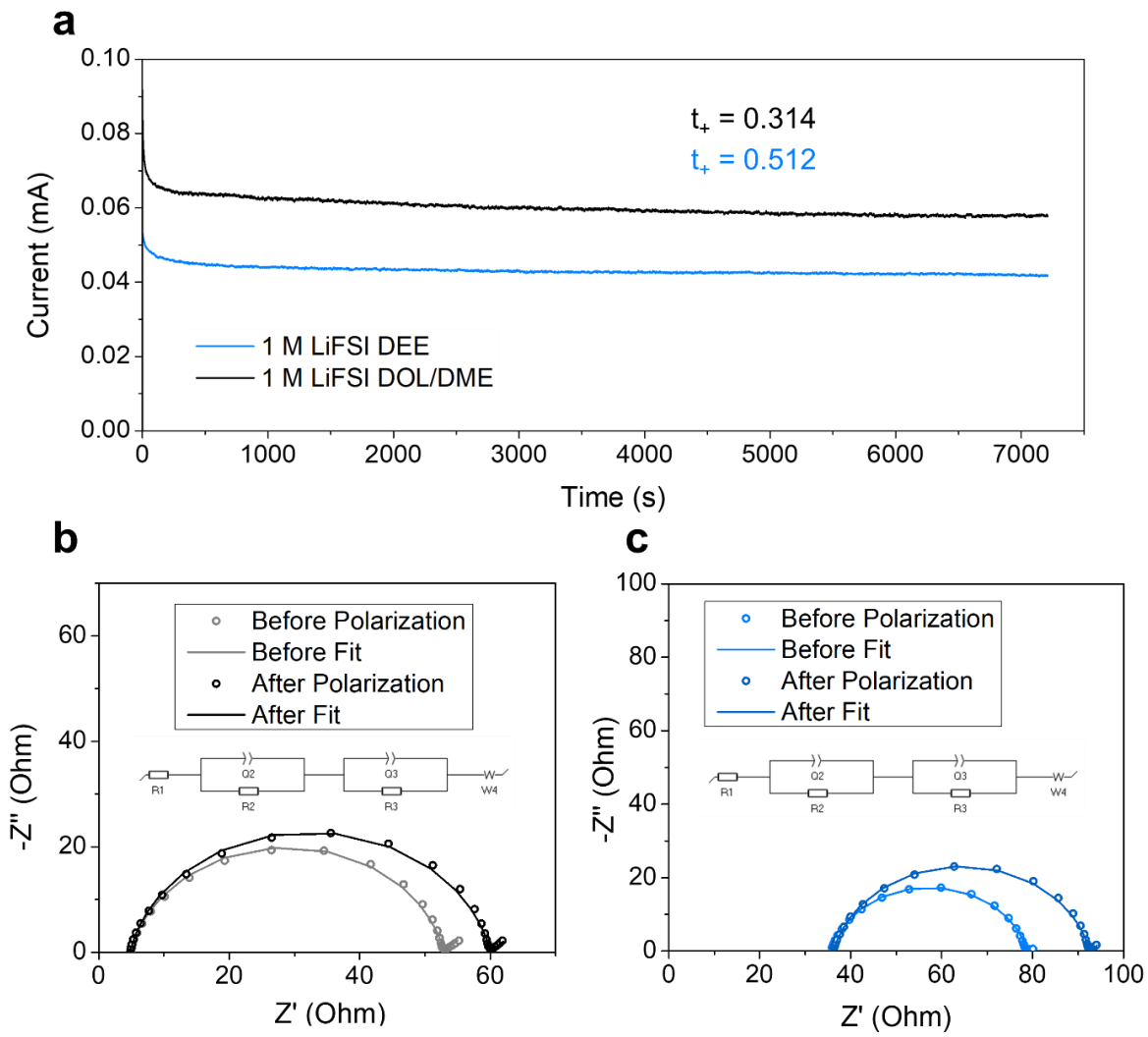

Supplementary Figure 6. Selected data for transference number calculations at room temperature. **a)** 5 mV polarization curves for the DEE and DOL/DME electrolytes. Nyquist impedance plots before and after polarization used for t_+ calculations of **b)** 1 M LiFSI DOL/DME, and **c)** 1 M LiFSI DEE.

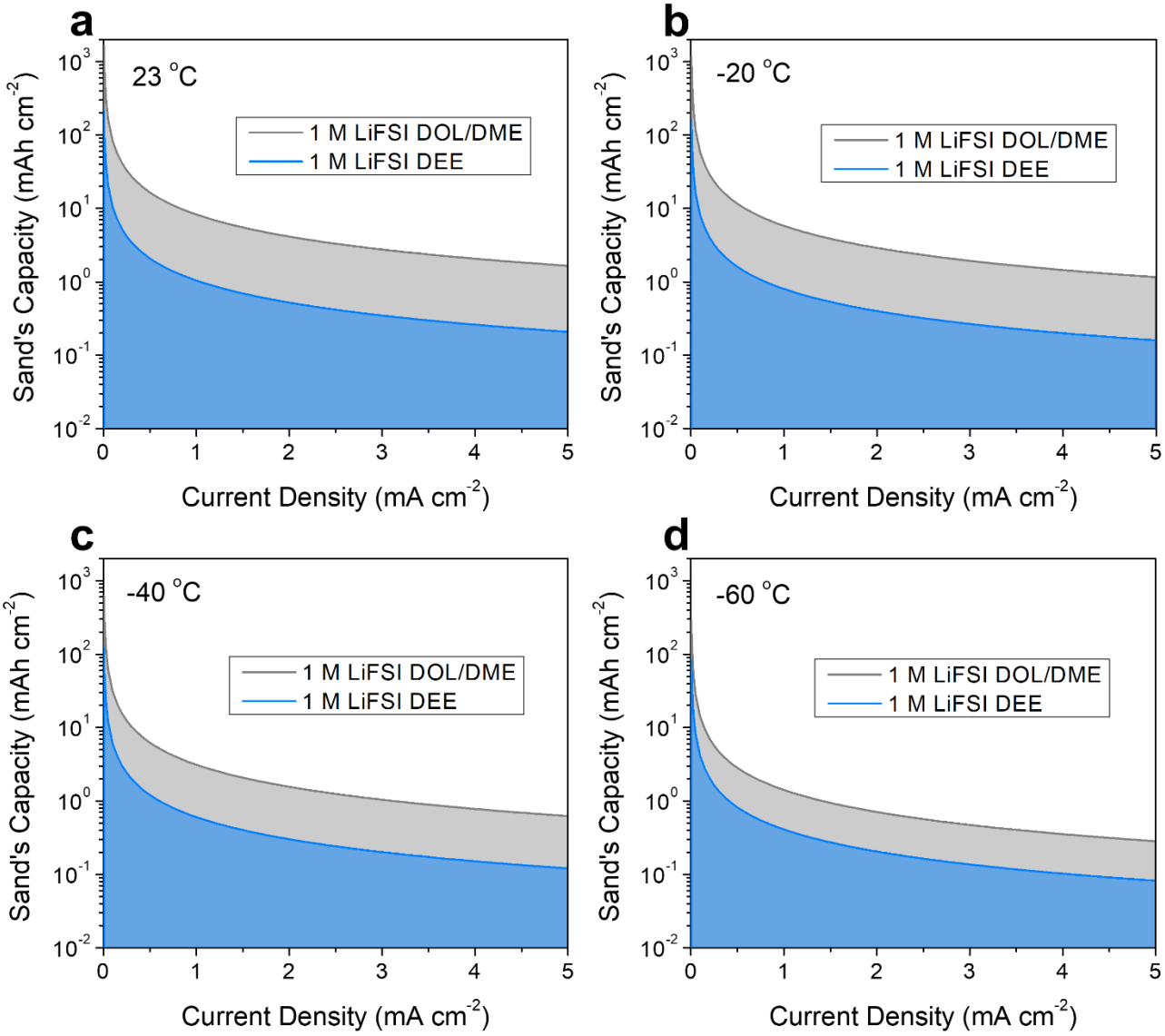

Supplementary Figure 7. Sand's capacity projections based on the ionic conductivity and transference numbers of the selected electrolytes at **a)** 23 °C, **b)** -20 °C, **c)** -40 °C, **d)** -60 °C. In all cases, the shaded area depicts the regime not limited by mass transfer.

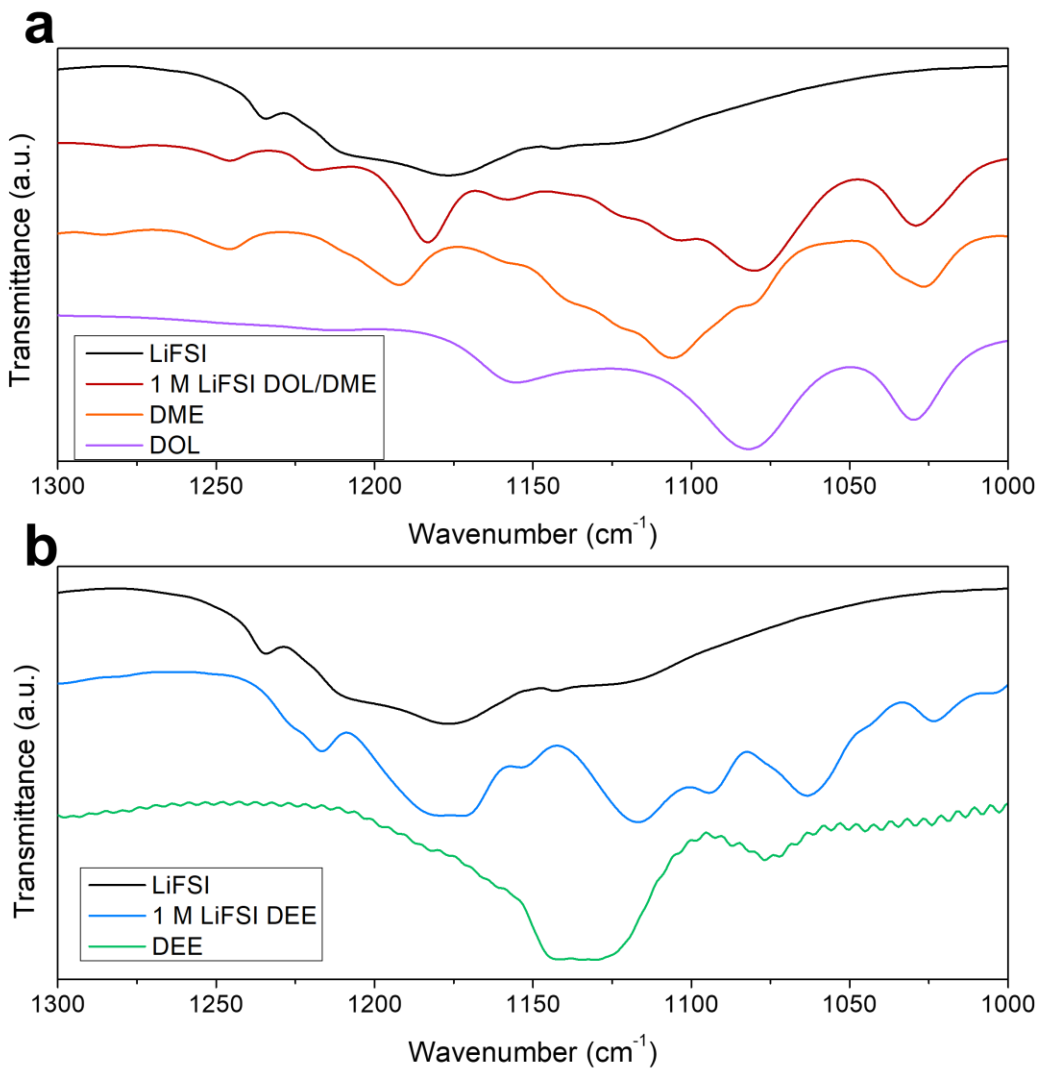

Supplementary Figure 8. FT-IR spectra of 1 M LiFSI electrolytes and their individual components.

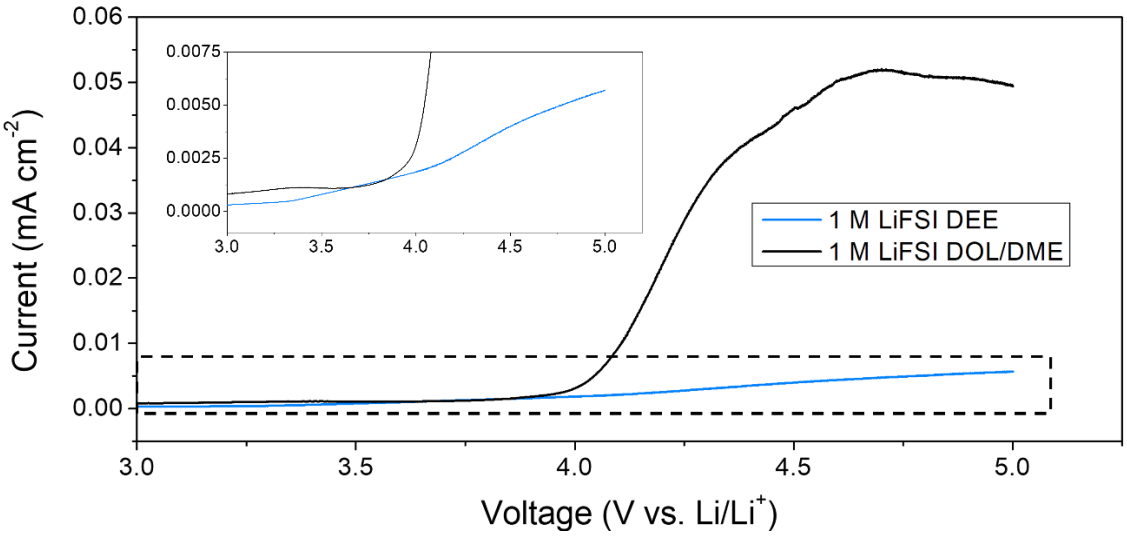

Supplementary Figure 9. Oxidative linear-scan voltammetry of the 1 M LiFSI DEE and 1 M LiFSI DOL/DME systems on Al working electrodes.

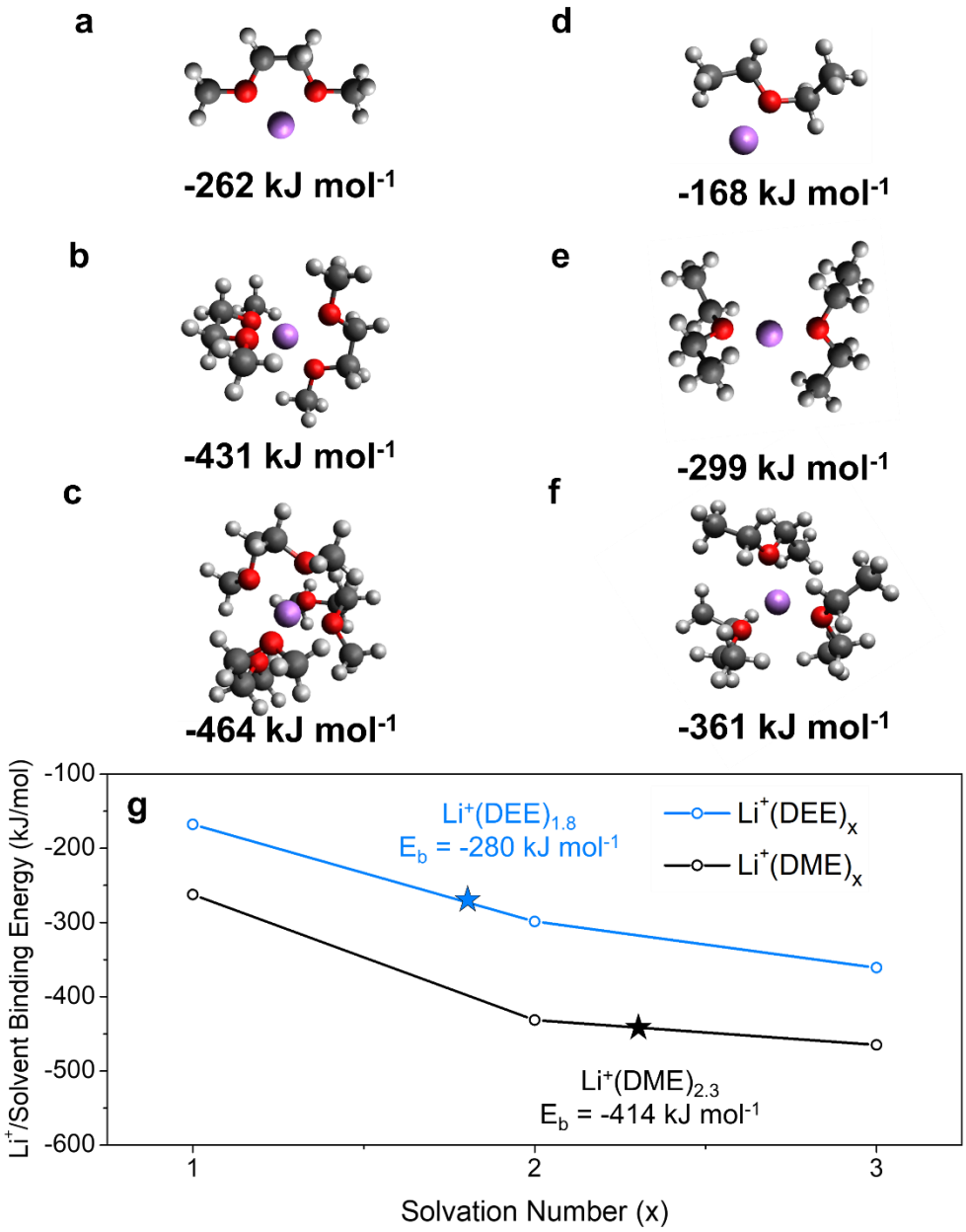

Supplementary Figure 10. Optimized structures and calculated binding energies of $Li^+(solvent)_n$ solvation complexes for: $Li^+(DME)_n$ **a)** n = 1, **b)** n = 2, **c)** n = 3, and $Li^+(DEE)_n$ **d)** n = 1, **e)** n = 2, **f)** n = 3. **g)** Corresponding binding energies for both systems. $Li^+(DEE)_{1.8}$ and $Li^+(DME)_{2.3}$ values were calculated via linear interpolation.

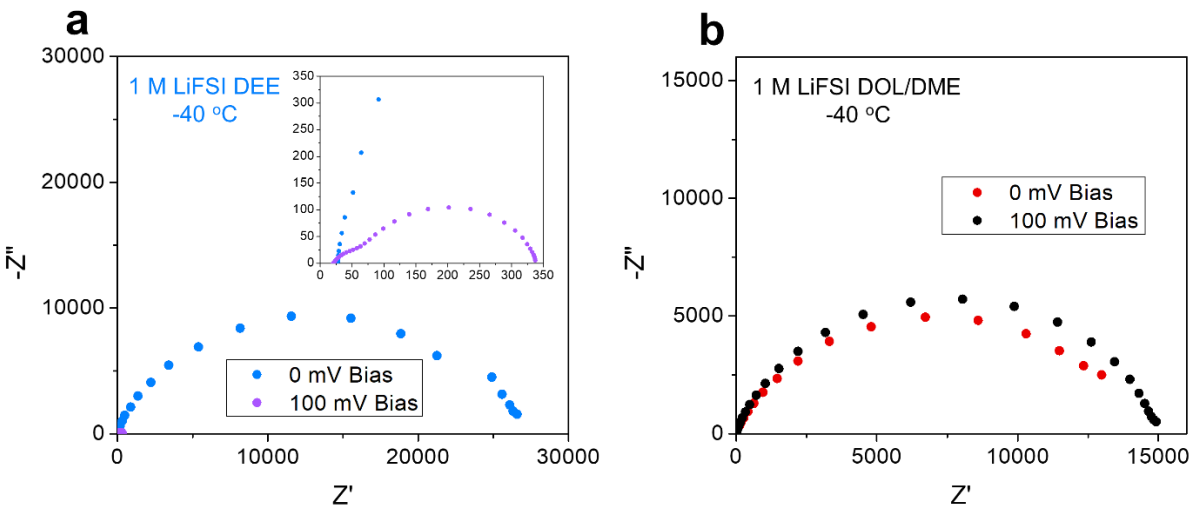

Supplementary Figure 11. Biased electrochemical impedance spectroscopy of Li||Li cells employing **a)** 1 M LiFSI DEE, and **b)** 1 M LiFSI DOL/DME at -40 °C. Due to the increased impedance at ultra-low temperatures, the EIS spectra with 0 mV bias corresponds to the nucleation impedance of the cell, whereas the spectra at 100 mV of bias corresponds to the impedance associated with charge transfer post nucleation.

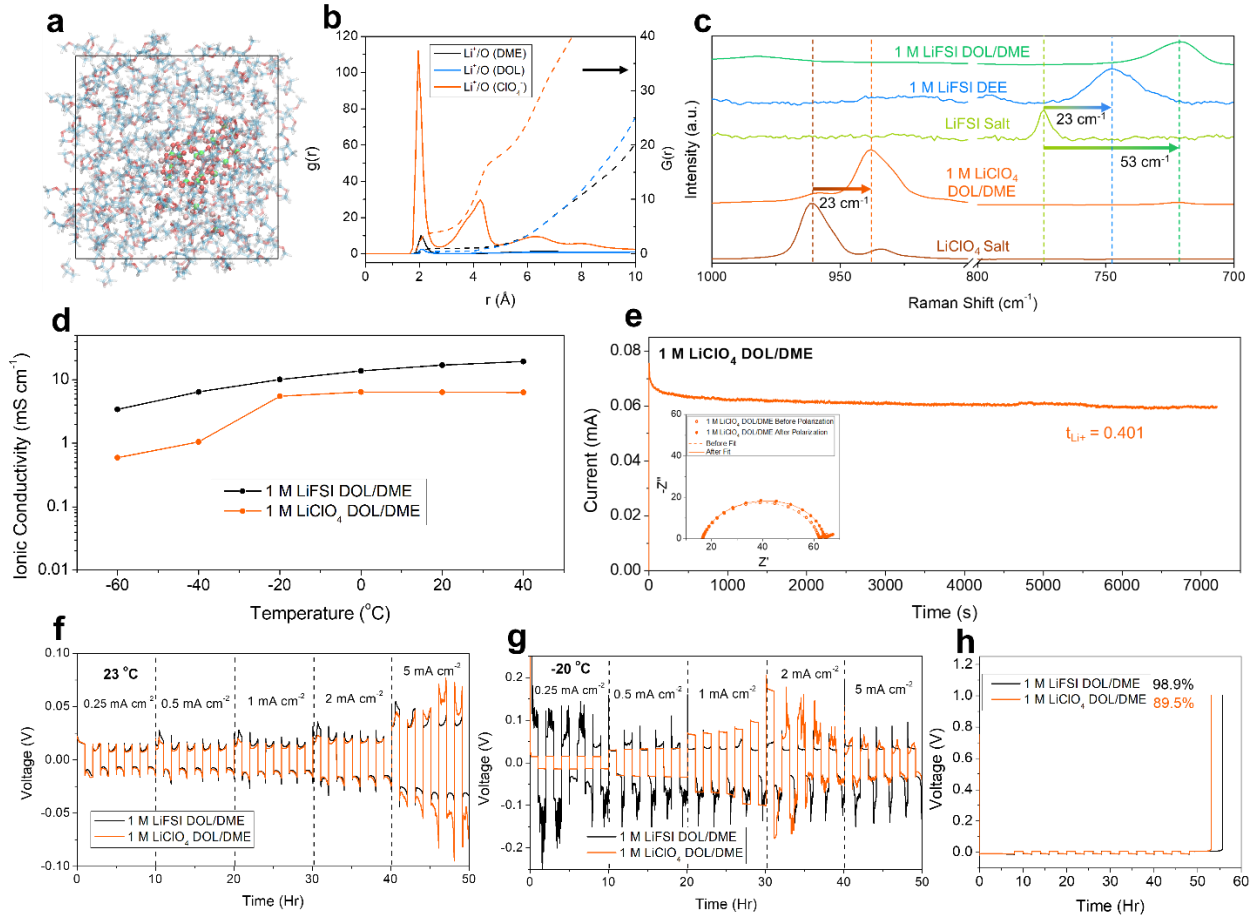

Supplementary Figure 12. Alteration of the solvation shell via anion selection, in this case $LiClO_4$. **a)** Snapshot and **b)** Li^+ radial distribution function obtained from MD simulation of 1 M $LiClO_4$ DOL/DME. **c)** Raman spectroscopy of 1 M $LiClO_4$ DOL/DME and $LiClO_4$ as compared to the LiFSI systems, where the O-Cl-O peak shift is indicative of a CIP structure. **d)** Ionic conductivity, and **e)** transference number measurements of the 1 M $LiClO_4$ DOL/DME electrolyte compared to 1 M LiFSI DOL/DME. **f)** Plating/stripping curves in symmetric Li||Li cells at **f)** 23°C, and **g)** -20 °C. The unstable voltages displayed are attributed to soft shorting events. **h)** Li CE measurements from Li/Cu cells.

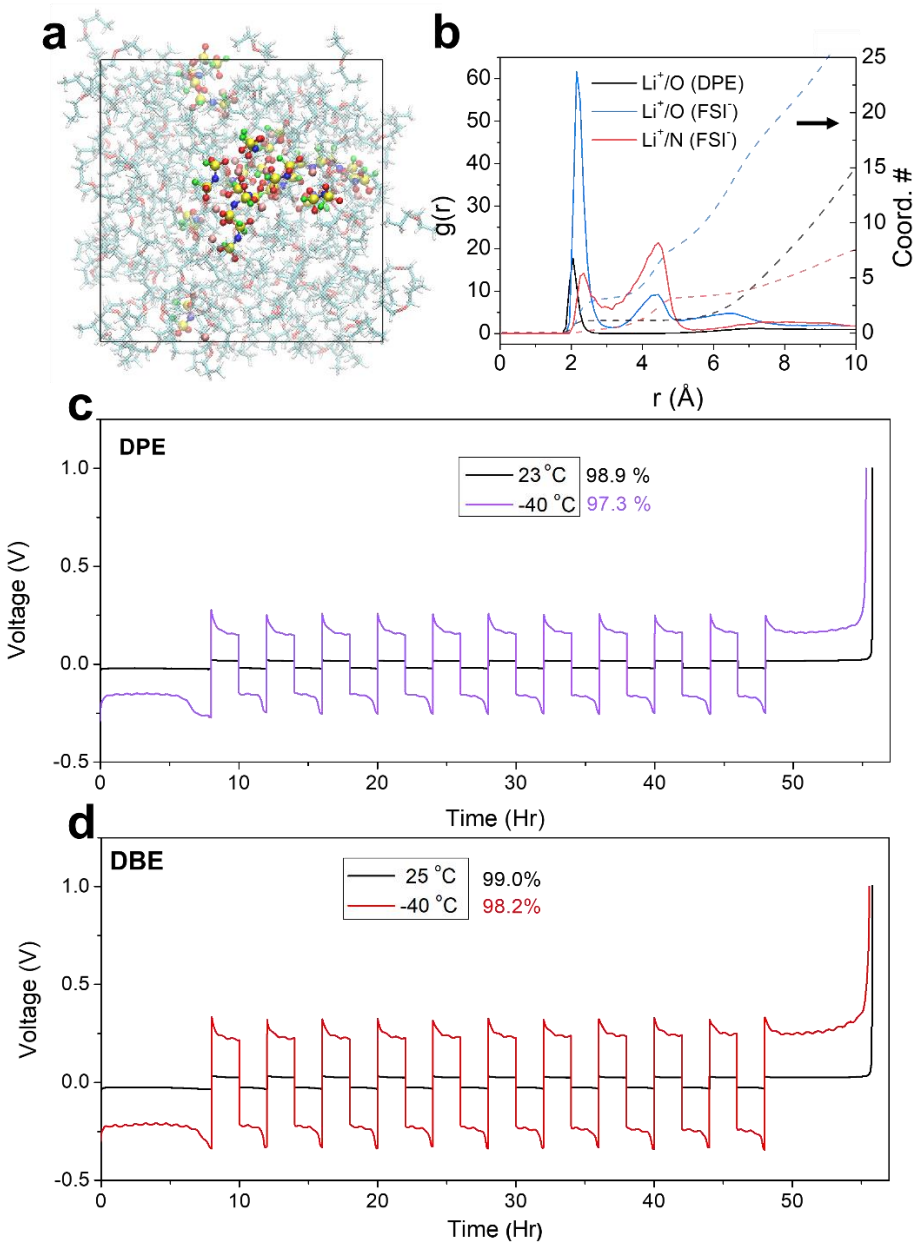

Supplementary Figure 13. Analysis of Li metal performance in monodentate ether electrolytes. **a)** Snapshot and **b)** Li^+ radial distribution function obtained from MD simulation of the DPE based electrolyte. Li CE measurements from Li||Cu cells employing **c)** DPE, and **d)** DBE based electrolytes.

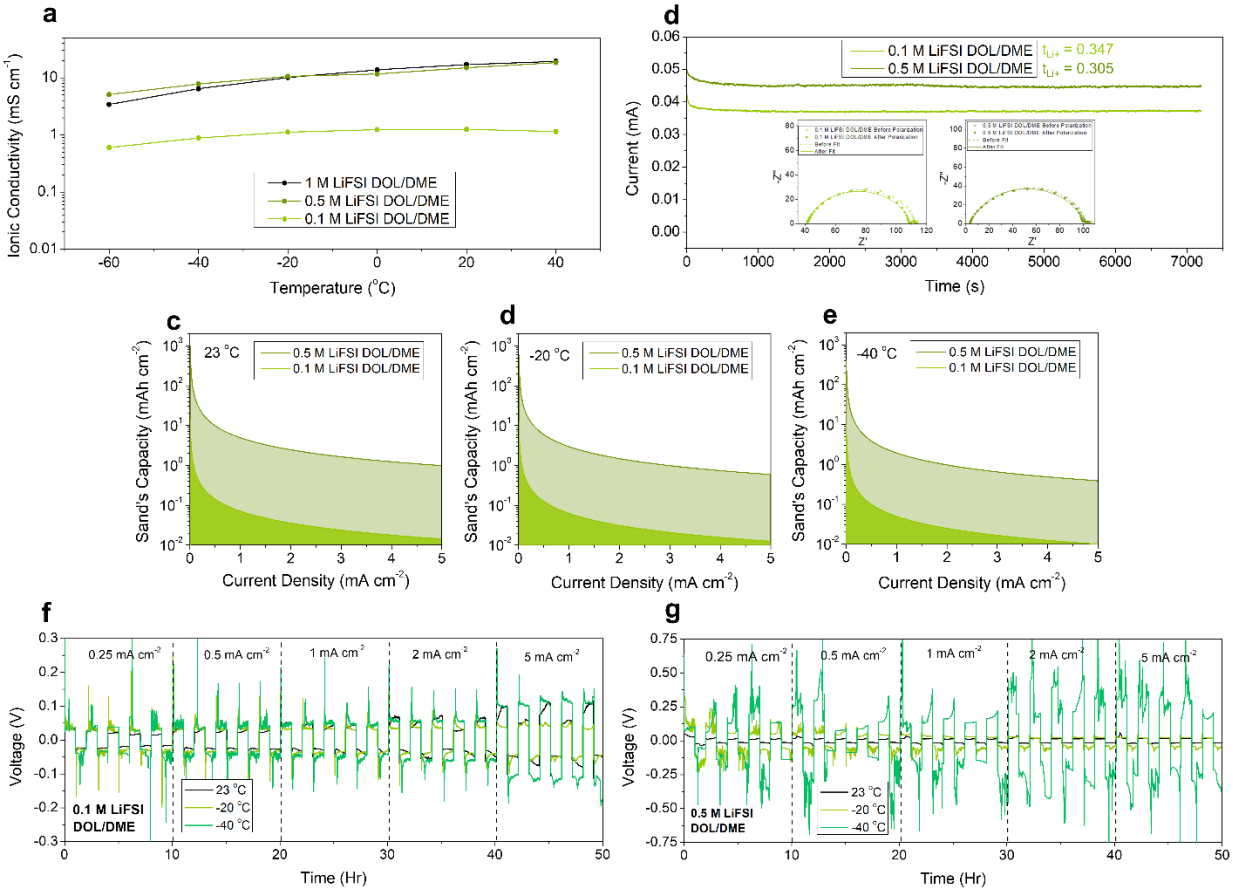

Supplementary Figure 14. Analysis of the FSI-DOL/DME electrolyte concentration series. **a)** Ionic conductivity and **b)** transference number measurements of the 0.1 M and 0.5 M LiFSI DOL/DME electrolytes. Sand's capacity projections of the electrolytes of interest at **c)** 23 °C, **d)** -20 °C, and **e)** -40 °C. **f)** Plating/stripping curves in symmetric Li||Li cells of **f)** 0.1 M LiFSI DOL/DME and **g)** 0.5 M LiFSI DOL/DME.

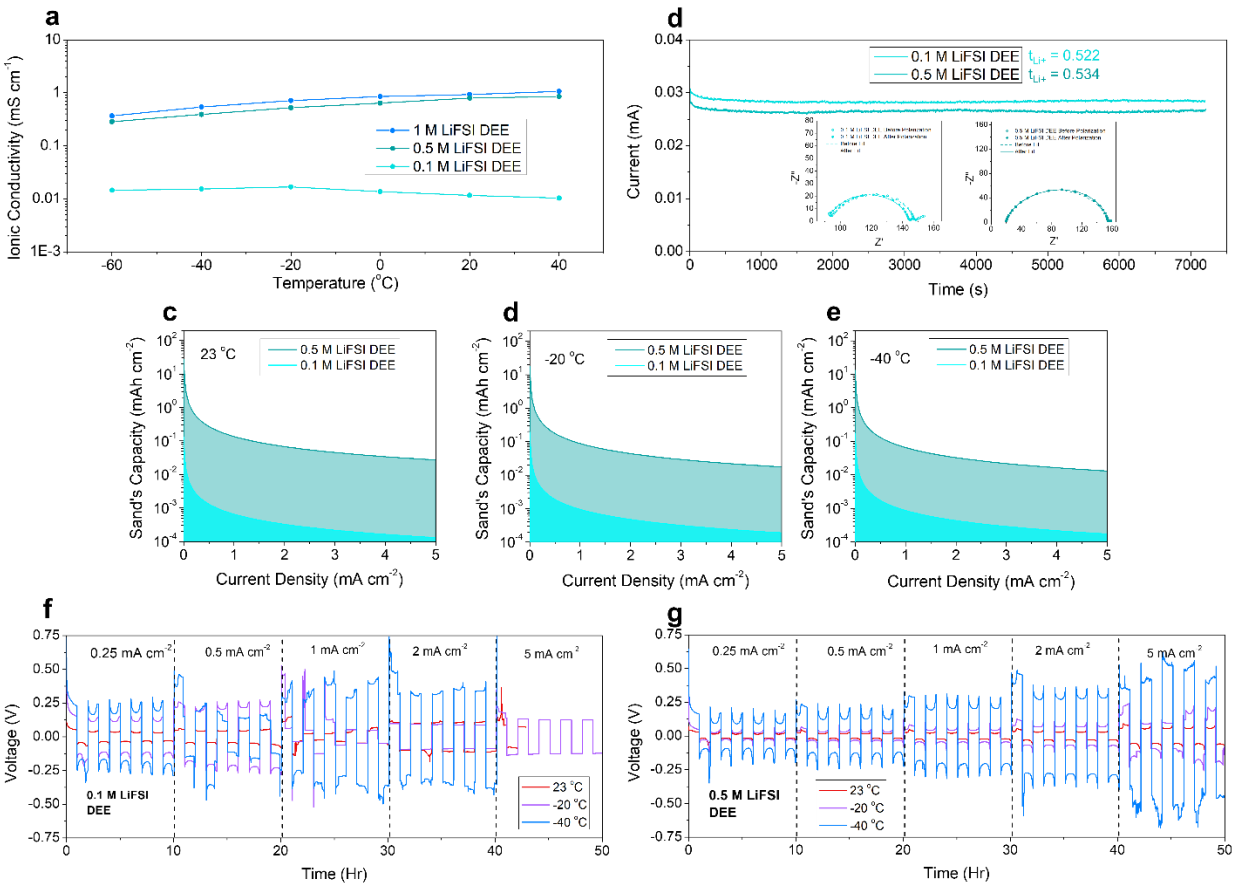

Supplementary Figure 15. Analysis of the FSI-DEE electrolyte concentration series. **a)** Ionic conductivity and **b)** transference number measurements of the 0.1 M and 0.5 M LiFSI DEE electrolytes. Sand's capacity projections of the electrolytes of interest at **c)** 23 ^{o}C, **d)** -20 ^{o}C, and **e)** -40 ^{o}C. **f)** Plating/stripping curves in symmetric Li||Li cells of **f)** 0.1 M LiFSI DEE and **g)** 0.5 M LiFSI DEE.

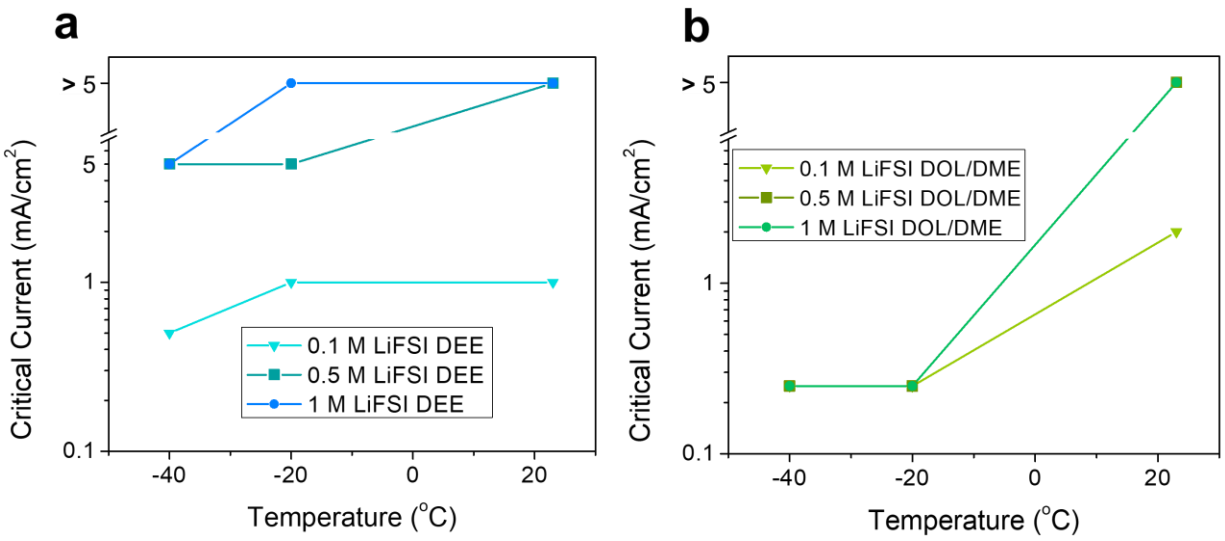

Supplementary Figure 16. Summarized critical current data from Li||Li cells employing 0.1, 0.5, and 1 M LiFSI in **a)** DEE and **b)** DOL/DME. The critical current is defined as the current at which shorting behavior is first observed.

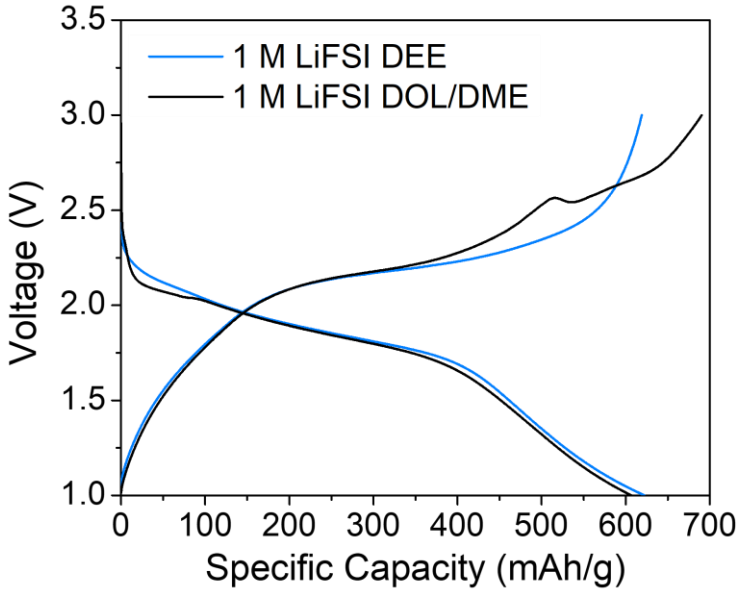

Supplementary Figure 17. Voltage profiles of 1x Li||SPAN full cells in the electrolytes of interest at room temperature.

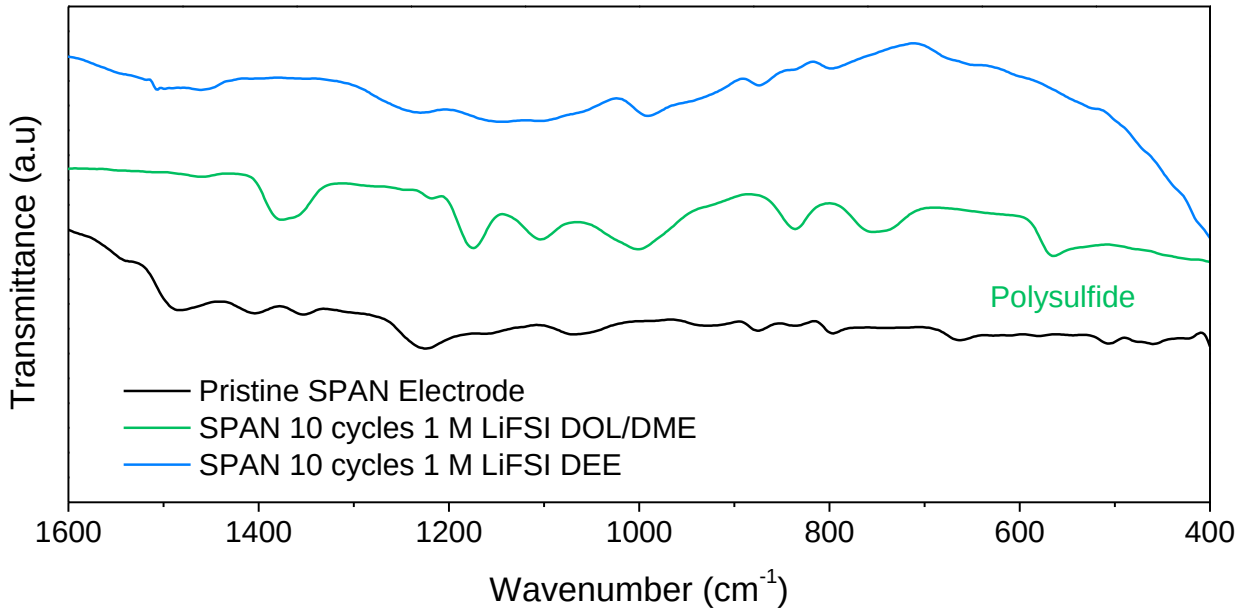

Supplementary Figure 18. FT-IR profiles of pristine SPAN electrodes and SPAN electrodes after 10 cycles in the electrolytes of interest.

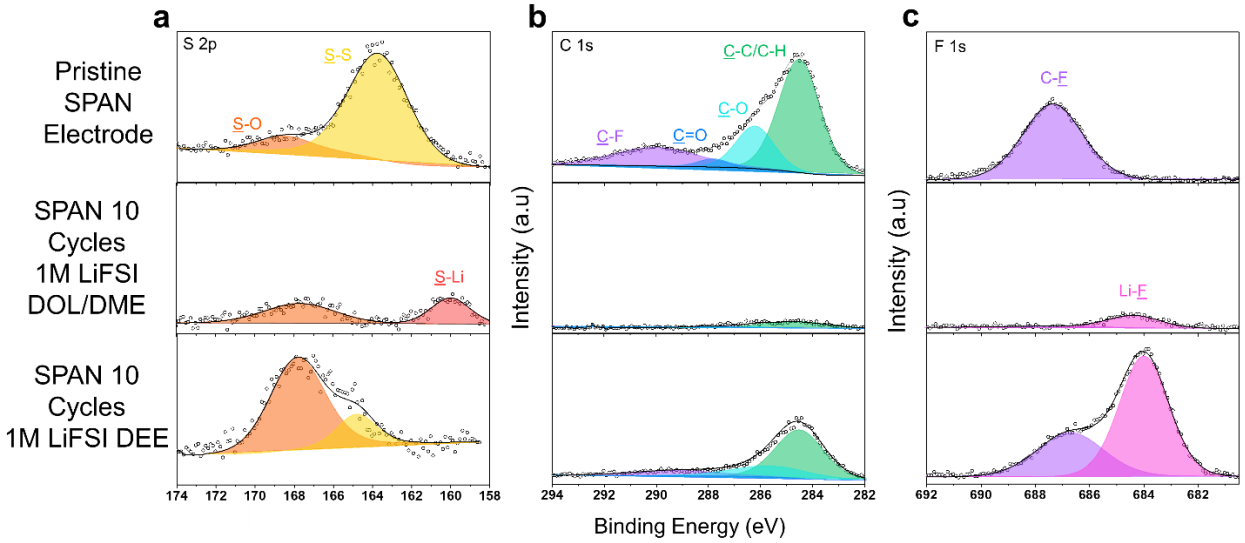

Supplementary Figure 19. Ex-situ XPS spectra of pristine SPAN electrodes and after 10 cycles in 1 M LiFSI DOL/DME and 1 M LiFSE DEE at room temperature. **a)** S 2p, **b)** C 1s, and **c)** F 1s.

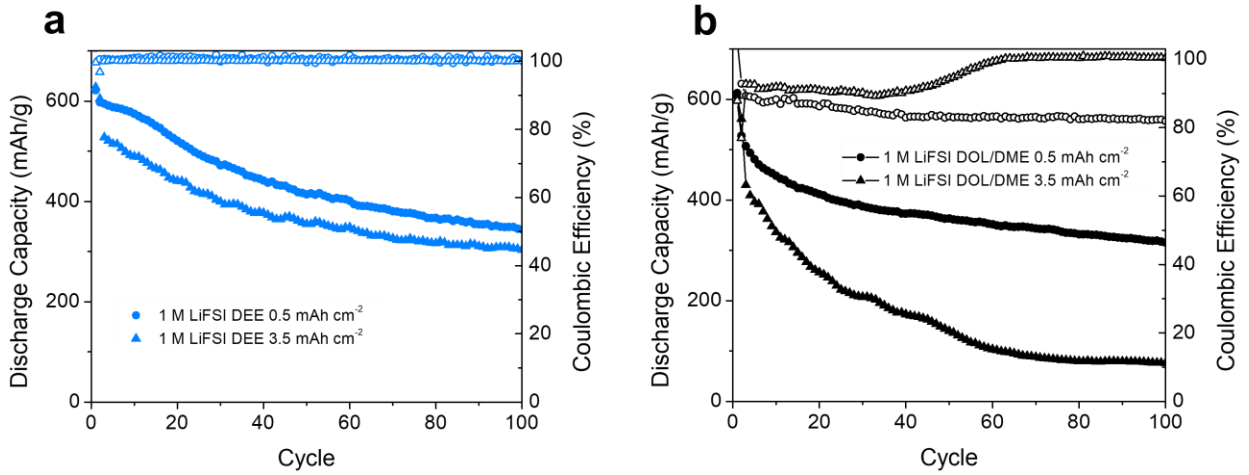

Supplementary Figure 20. Room temperature cycling data of Li||SPAN half cells at high and low mass loadings in **a)** 1 M LiFSI DEE, and **b)** 1 M LiFSI DOL/DME at 25°C.

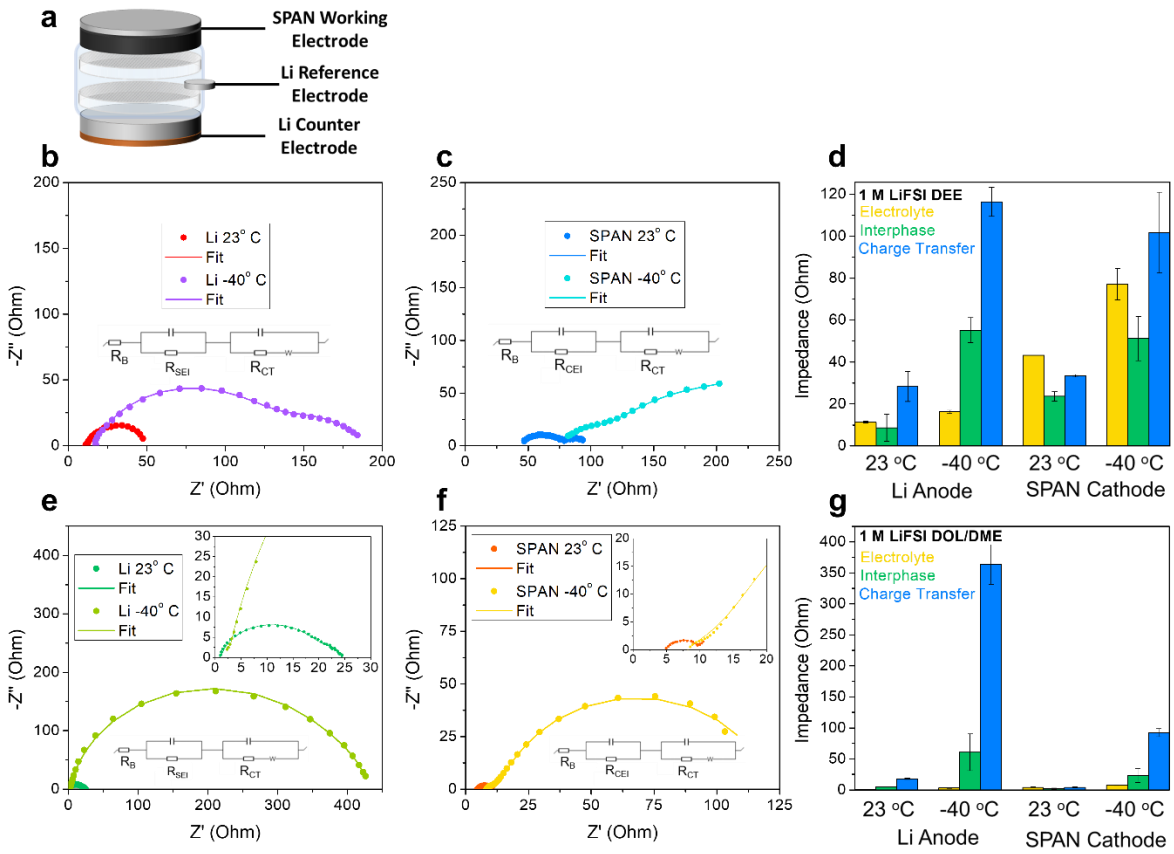

Supplementary Figure 21. 3-Electrode impedance study of SPAN||Li||Li cells at 23 °C and -40 °C. **a)** Working schematic of the 3 electrode cell. Impedance spectra of the **b)** Li anode, **c)** SPAN cathode in 1 M LiFSI DEE at 50% state-of-charge (SOC). **d)** breakdown of equivalent circuit elements from fit. Impedance spectra of the **e)** Li anode, **f)** SPAN cathode in 1 M LiFSI DOL/DME at 50% SOC. **g)** breakdown of equivalent circuit elements from fit, where the error bars represent one standard deviation of resistance values obtained from curve fitting. EIS spectra were taken directly following discharge to 50% SOC to avoid nucleation impedance.

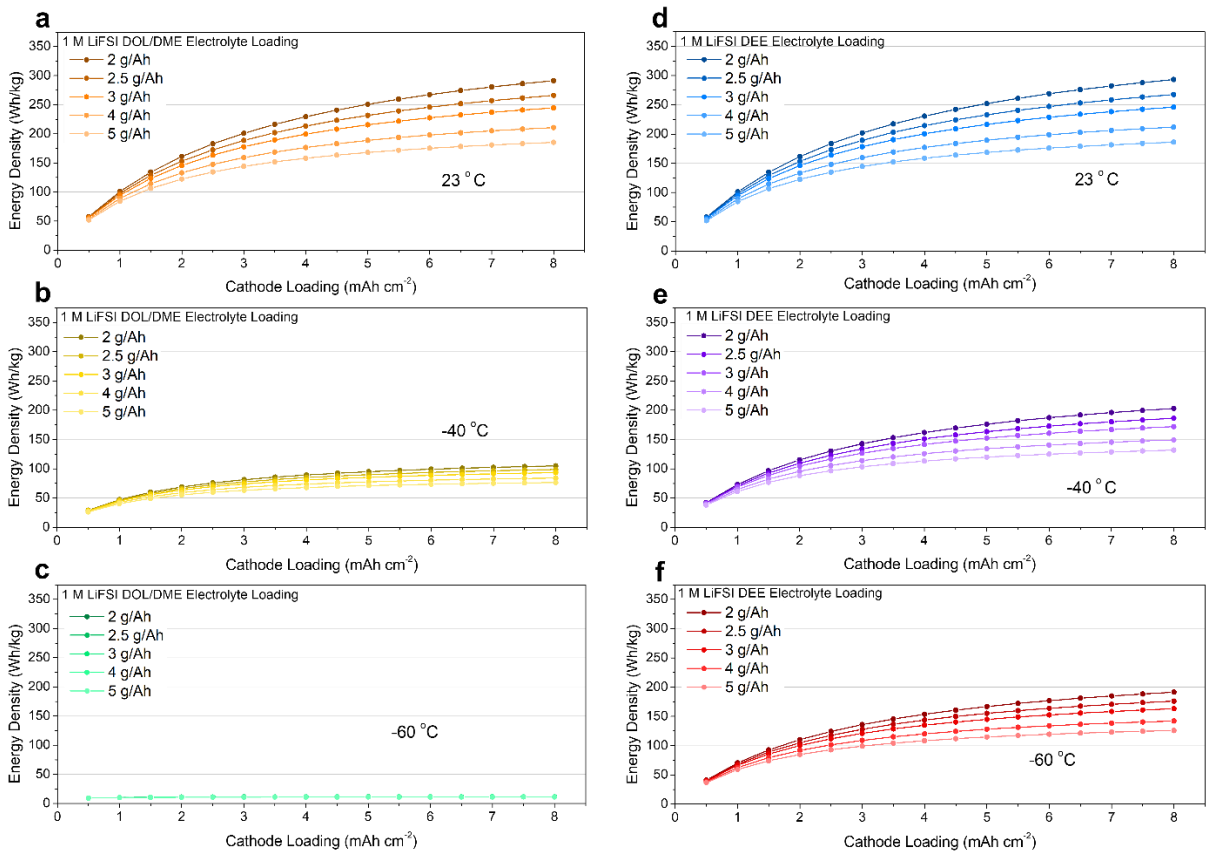

Supplementary Figure 22. Energy density projections for the 1x Li||SPAN full cells at various cathode and electrolyte loadings. In 1 M LiFSI DOL/DME at **a)** 23 ºC, **b)** -40 ºC, **c)** -60 ºC. In 1 M LiFSI DEE at **d)** 23 ºC, **e)** -40 ºC, **f)** -60 ºC.

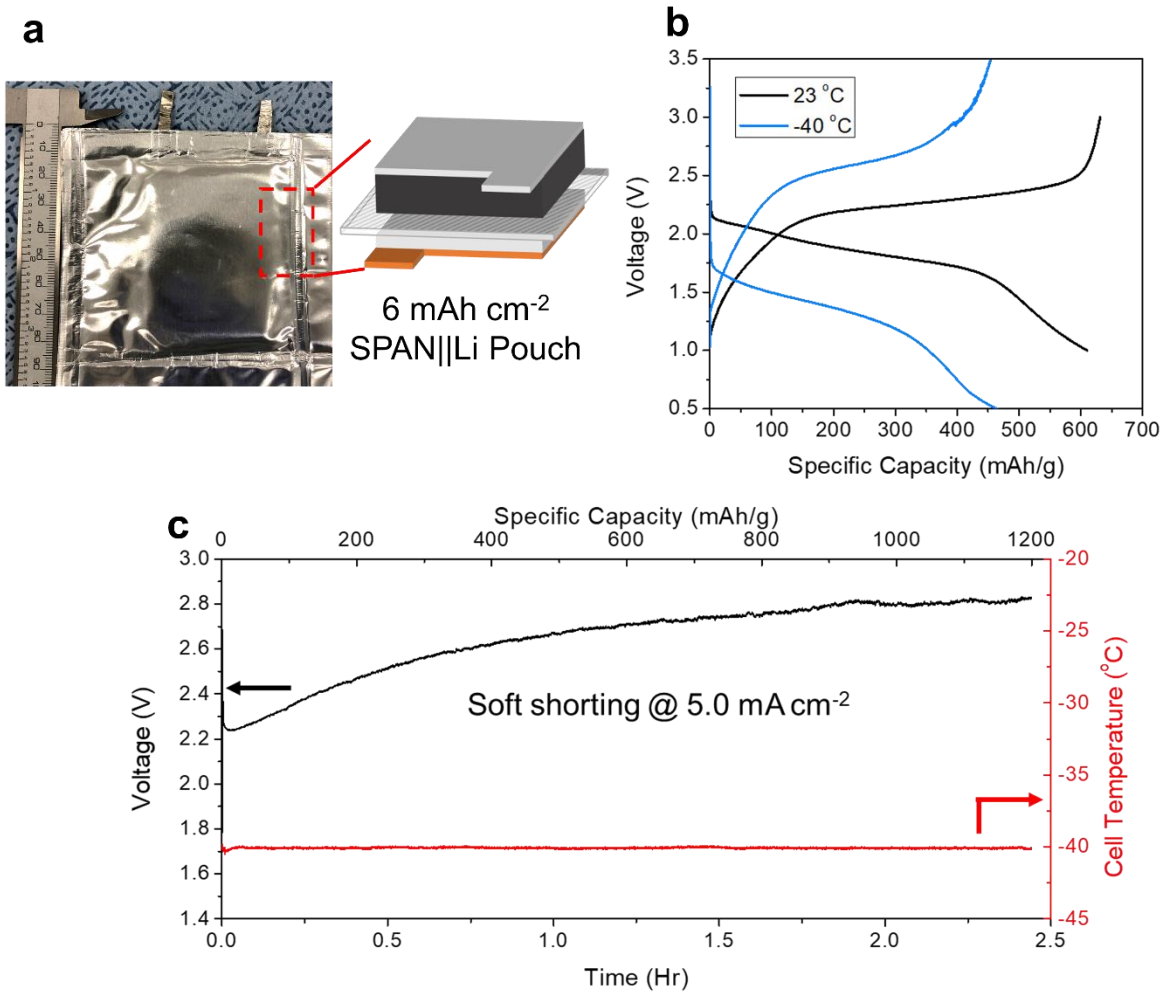

Supplementary Figure 23. Pouch cell demonstration for scaling feasibility and low-temperature safety. **a)** Photograph and schematic of pouch cell design. **b)** Charge/discharge curves at various temperatures under 0.5 mA cm^{-2}. **c)** Soft shorting experiment with simultaneous measured cell temperature. The slight fluctuations of the cell temperature correspond to the compressor cycling of the temperature chamber.

Supplementary Table 3. Metrics of interest for previously published low temperature Li metal batteries. Cathode loading in this case is equivalent to the capacity passed per cycle.

	Li Metal Loading	Cathode Loading	Li Passed Per Cycle	Low Temperature Discharging	Low Temperature Charging	Low Temp. Capacity Retention
Rustomiji *et al.*[3]	229x Excess	0.9 mAh cm^{-2}	0.43 %			61% at -60 ^{o}C
Dong *et al.*[4]	206x Excess	0.25 mAh cm^{-2}	0.48 %			68% at -70 ^{o}C
Fan *et al.*[5]	26x Excess	2 mAh cm^{-2}	3.7 %			80% at -61 ^{o}C
Holoubek *et al.* [6]	2.6x Excess	1.3 mAh cm^{-2}	27.8 %			67% at -60 ^{o}C
This Work	1x Excess	3.5 mAh cm^{-2}	50 %			76% at -60 ^{o}C

References

[1] D. R. L.-T. J. B.-T. & F. Group, *CRC Handbook of Chemistry and Physics, 95th Edition, CRC Press, 2014: CRC Handbook of Chemistry and Physics*, **2014**.

[2]Marcus, R. A. On the Theory of Oxidation-Reduction Reactions Involving Electron Transfer. I. *J. Chem. Phys.* **24**, 966–978 (1956).

[3] C. S. Rustomji, Y. Yang, T. K. Kim, J. Mac, Y. J. Kim, E. Caldwell, H. Chung, Y. S. Meng, *Science* **2017**, *356*, eaal4263.

[4] X. Dong, Y. Lin, P. Li, Y. Ma, J. Huang, D. Bin, Y. Wang, Y. Qi, Y. Xia, *Angewandte Chemie International Edition* **2019**, *58*, 5623–5627.

[5] X. Fan, X. Ji, L. Chen, J. Chen, T. Deng, F. Han, J. Yue, N. Piao, R. Wang, X. Zhou, et al., *Nature Energy* **2019**, *4*, 882–890.

[6] Holoubek, J. *et al.* An All-Fluorinated Ester Electrolyte for Stable High-Voltage Li Metal Batteries Capable of Ultra-Low-Temperature Operation. *ACS Energy Lett.* 1438–1447 (2020).